Magnetostriction, Soft Magnetism, and Microwave Properties in Co-Fe-C Alloy Films

Jiawei Wang,[1,2,*] Cunzheng Dong,[2] Yuyi Wei,[2] Xianqing Lin,[1] Benson Athey,[3] Yunpeng Chen,[4]
Andrew Winter,[5] Gregory M. Stephen,[5] Don Heiman,[5] Yifan He,[2] Huaihao Chen,[2] Xianfeng Liang,[2]
Chengju Yu,[2] Yujia Zhang,[6] Elizabeth J. Podlaha-Murphy,[6] Mingmin Zhu,[2,7] Xinjun Wang,[2] Jun Ni,[8]
Michael McConney,[3] John Jones,[3] Michael Page,[3] Krishnamurthy Mahalingam,[3] and Nian X. Sun[2,†]

[1] *College of Science, Zhejiang University of Technology, Hangzhou 310023, China*
[2] *Department of Electrical and Computer Engineering, Northeastern University, Boston, Massachusetts 02115, USA*
[3] *Air Force Research Laboratory, Wright-Patterson AFB, Ohio 45433, USA*
[4] *Winchester Technologies, LLC, Burlington, Massachusetts 01803, USA*
[5] *Department of Physics, Northeastern University, Boston, Massachusetts 02115, USA*
[6] *Department of Chemical and Biomolecular Engineering, Clarkson University, Potsdam, New York 13699, USA*
[7] *Key Laboratory of Electromagnetic Wave Information Technology and Metrology of Zhejiang Province, College of Information Engineering, China Jiliang University, Hangzhou 310018, China*
[8] *State Key Laboratory of Low-Dimensional Quantum Physics and Collaborative Innovation Center of Quantum Matter, Department of Physics, Tsinghua University, Beijing 100084, China*

(Received 24 July 2019; published 9 September 2019)

In the past decades, ferromagnet-metalloid alloy films of Co-Fe-B have been widely used in alternative magnetic devices due to their excellent performance, such as easy industrial-scale fabrication, considerable ability for tunneling magnetoresistance and perpendicular magnetic anisotropy. However, the insufficient thermal tolerance and interfacial state densities in the typical Co-Fe-B/MgO system limits the devices' optimization. Because of the improvement in thermal stability and interfacial properties by carbon element replacement, alternative theoretical and experimental work on Co-Fe-C alloy film properties have been reported. Here, we report on the magnetostrictive behavior, soft magnetism, and microwave properties of a series of $(\mathrm{Co}_{0.5}\mathrm{Fe}_{0.5})_x\mathrm{C}_{1-x}$ films grown on silicon (001) substrates. The addition of carbon changes the Co-Fe-C films from nanocrystalline body-centered-cubic to an amorphous phase and leads to a high saturated magnetostriction constant of 75 ppm, high piezomagnetic coefficient of 10.3 ppm/Oe, excellent magnetic softness with a low coercivity less than 2 Oe, narrow ferromagnetic resonance line width of 25 Oe at the X band, extremely low Gilbert damping of 0.002, and up to 500 °C thermal stability. The large saturated magnetostriction constant and piezomagnetic coefficient result from the coexistence of nanocrystalline body-centered-cubic and amorphous phases. The extremely low Gilbert damping is related to the minimized density of states around the Fermi energy of the alloys induced by carbon doping. The combination of these properties makes Co-Fe-C films promising candidates to be widely used in voltage-tunable magnetoelectric devices and microwave magnetic devices.

DOI: 10.1103/PhysRevApplied.12.034011

I. INTRODUCTION

In recent decades, the development of different magnetic devices such as spin-transfer-torque random-access memory (STT RAM) or spin-torque oscillators [1,2], requires the magnetic properties of each layer to be precisely tuned according to the specifics of the application. The traditional ferromagnetic metals, Fe, Co, and Ni, have large ferromagnetic moments and can be easily fabricated as bulk or films with high purity. However, they have rigid magnetic $3d$ electron occupation and electronic band structure, which make them difficult to be tuned except by extreme avenues such as a considerably large electric field [3,4]. Thus, the modulation of magnetic properties of these materials is limited. This problem can be solved in binary alloy systems. For example, in the $\mathrm{Ni}_x\mathrm{Fe}_{1-x}$ and $\mathrm{Co}_x\mathrm{Fe}_{1-x}$ alloy systems, transitions occur from a body-centered-cubic (bcc) to a face-centered-cubic (fcc) phase. Such phase transitions result in a nontrivial change in the

---

[*] wangjiawei@zjut.edu.cn
[†] n.sun@northeastern.edu

electronic band structure, which can be seen as additional features in the Slater-Pauling curve [5,6]. In addition, extraordinary behaviors can be achieved around the phase boundary, such as a giant magnetostriction as large as 260 ppm observed in a textured $\mathrm{Co}_x\mathrm{Fe}_{1-x}$ system [7].

The conventional binary alloys of $\mathrm{Ni}_x\mathrm{Co}_{1-x}$, $\mathrm{Ni}_x\mathrm{Fe}_{1-x}$, and $\mathrm{Co}_x\mathrm{Fe}_{1-x}$ were thoroughly investigated in bulk samples during the 1960s and 1970s [8–10]. But many emerging technologies require films of these materials. Industrial-scale fabrication of magnetic devices requires homogeneous thin-film growth over large surface areas via magnetron sputtering. It has been found that doping metalloid elements into a binary alloy matrix is superior to simple binary alloys in forming smooth layers over large areas [11,12]. The light elements such as B, Si, and N often break down the crystalline phase of binary alloys, forming a uniform amorphous structure [13]. A successful case was the ferromagnet-metalloid alloy Co-Fe-B because of its perfect soft ferromagnetism [14] without magnetocrystalline anisotropy, high spin polarization [15], and considerable large tunneling magnetoresistance (TMR) in magnetic tunnel junctions (MTJs) [16].

To date, Co-Fe-B alloys have been widely used in designing parallel and perpendicular anisotropy MTJs with a MgO tunneling barrier. However, the thermal stability of a Co-Fe-B alloy film is still a key obstacle. For example, current-induced magnetization switching in the perpendicular anisotropy STT RAM is of great interest because of its small threshold current density and good thermal stability [17]. But a postannealing process is necessary to enhance TMR and integrate STT RAM in perpendicular MTJs' design. It was found that the perpendicular anisotropy drastically decreased when the annealing temperature was over 350 °C [18]. Thus, the perpendicular anisotropy system can only work in a limited temperature range for annealing. There have been a few reports on experimental works that the thermal stability of ferromagnetic materials could be effectively improved by doping with carbon atoms. El-Gendy *et al.*'s work showed that the Co-Fe-carbide nanoparticles had a larger thermal stability than commonly used materials [19]. Recently, Chen *et al.*'s experiments showed $\mathrm{Co}_{0.4}\mathrm{Fe}_{0.4}\mathrm{C}_{0.2}$ alloy films provided better thermal tolerance, higher perpendicular anisotropy critical thickness, and an analogous intrinsic damping constant with $\mathrm{Co}_{0.4}\mathrm{Fe}_{0.4}\mathrm{B}_{0.2}$ films [20]. Moreover, the theoretical calculation from Chen *et al.* [21] made the suggestion that C-doped MTJ was predicted to have a significantly higher TMR than the B-doped MTJ due to its higher interfacial state densities in the Co-Fe-X/MgO interface. Thus, the Co-Fe-C alloy is a promising candidate that could be more widely used than the Co-Fe-B alloy. But the magnetic properties of alloys are always held to the composition-dependent rule. Thus, the composition dependence of the ferromagnetic properties of Co-Fe-C is highly desired. Because the $\mathrm{Co}_{0.4}\mathrm{Fe}_{0.4}\mathrm{B}_{0.2}$ composition was used in most research regarding its lowest intrinsic damping constant and highest tunneling spin polarization in the Co-Fe-B alloys [15], $(\mathrm{Co}_{0.5}\mathrm{Fe}_{0.5})_x\mathrm{C}_{1-x}$ was chosen in our study due to its compositional similarity. So far, there have been no reports on carbon content- (CC) dependent magnetostriction, magnetism, and microwave properties in $(\mathrm{Co}_{0.5}\mathrm{Fe}_{0.5})_x\mathrm{C}_{1-x}$ alloy films.

In this paper, we study magnetostriction, soft magnetism, and microwave properties of different CCs in a series of $(\mathrm{Co}_{0.5}\mathrm{Fe}_{0.5})_x\mathrm{C}_{1-x}$ films grown on a silicon (001) substrate. It is shown that a combination of high saturation magnetostriction constant (λ_s), high piezomangetic coefficient ($d\lambda/dH$), very low coercivity, narrow ferromagnetic resonance (FMR) line width, low Gilbert damping constant, and high thermal stability are achieved. The notable result is that λ_s is larger than the value in Ga-Fe-B alloys [22] and three times larger than in Co-Fe-B alloys [23]. The minimum in-plane Gilbert damping is 0.002. All of these properties make Co-Fe-C films attractive for voltage-tunable magnetoelectric devices in multiferroic composite structures and other microwave magnetic devices.

II. EXPERIMENTAL DETAILS

A. Sample preparation

Multilayers structures of $\mathrm{Ta}(5)/(\mathrm{Co}_{0.5}\mathrm{Fe}_{0.5})_x\mathrm{C}_{1-x}(20)/\mathrm{Ta}(5)$ (in nm) with various CCs are sputtered onto (001)-oriented $6 \times 6\ \mathrm{mm}^2$ silicon substrates using two separate targets of $\mathrm{Co}_{0.5}\mathrm{Fe}_{0.5}$ and carbon. The Si (001) substrate is naturally oxidized with an oxide thickness of 1–2 nm. The CC of the $(\mathrm{Co}_{0.5}\mathrm{Fe}_{0.5})_x\mathrm{C}_{1-x}$ films is varied by changing the carbon target power while keeping the $\mathrm{Co}_{0.5}\mathrm{Fe}_{0.5}$ target power at 30 W on the 2-inch-diameter targets. The $(\mathrm{Co}_{0.5}\mathrm{Fe}_{0.5})_x\mathrm{C}_{1-x}$ films are deposited in a 3 mTorr Ar atmosphere in a vacuum chamber with a base pressure better than 1×10^{-7} Torr.

B. Experimental characterization

The respective deposition rate and the crystal structures are examined by x-ray reflectivity (XRR) and x-ray diffraction (XRD) using a Bruker D8 high-resolution diffractometer with Cu K_α radiation. The $(\mathrm{Co}_{0.5}\mathrm{Fe}_{0.5})_x\mathrm{C}_{1-x}$ films' compositions are characterized by x-ray photoelectron spectroscopy (XPS) on CMSE's PHI Versaprobe II. Fast Fourier transform (FFT) analysis in the high resolution transmission electron microscope (HRTEM) is employed for $(\mathrm{Co}_{0.5}\mathrm{Fe}_{0.5})_x\mathrm{C}_{1-x}$ films' crystallization nature. Magnetostriction constants are measured using Si machined cantilevers with the largest drive magnetic field up to 300 Oe and the best resolution of 0.1 ppm. Before measurement, a large magnetic field along the in-plane magnetic easy axis (MEA) is used to saturate the sample. The cantilever's bending is monitored when an ac magnetic field is applied along the in-plane magnetic hard axis (MHA). A standard sample of a 100-nm $Ga_{0.176}Fe_{0.704}B_{0.12}$ film with $\lambda_s = 70$ ppm [22] is used to calibrate the system (instrument details are introduced in Ref. [24]). Magnetization versus magnetic field *M-H* curves are measured using a Quantum Design SQUID Magnetic Properties Measurement System (MPMS) and Vibrating Sample Magnetometer (VSM). Microwave properties are characterized using a homemade broadband apparatus equipped with an adjustable frequency of 0.01–26 GHz FMR spectrometer.

III. RESULTS AND DISCUSSION

A. Structure and composition

XRD and XPS measurements are carried out to characterize the structure and composition of the films. Figure 1(a) shows that bcc (110) reflection from $Co_{0.5}Fe_{0.5}$ can be seen in the Co-Fe-C films with low CC. The signal-to-noise ratio (SNR) analysis after normalizing the Si substrate (004) reflection in the Supplemental Material S1 [25] indicates that the doping carbon atoms in the $Co_{0.5}Fe_{0.5}$ alloy decrease the (110) reflection intensity, leading to refined grain size and a more disordered lattice. This result matches what has been observed in Ga-Fe-B and Co-Fe-B films [15,22]. To characterize the films' crystallization nature with CC, a rocking curve of (110) reflection is employed as shown in Fig. 1(b). The accurate full width at half maximum (FWHM) is obtained using the Gauss peak function fitting as the dashed curves in Fig. 1(b). The dotted curves are guided to realize the broadening process of FWHM with the CC increase. The FWHMs of Co-Fe-C films are collected in Fig. 1(c) as red balls. The grain sizes of the Co-Fe-C alloy films with low CC are obtained using the Debye-Scherrer model [35] as black balls in Fig. 1(c). Both the SNR and grain size analyses in the Supplemental Material S1 [25] and Fig. 1(c) reveal that the transition of grain size and the lattice disorder are gradual. Moreover, the values of SNR and grain size approach the minimum limits (SNR equals 1, grain size equals 2–3 nm [36]) when the CC reaches around 4%, suggesting that 4% is a critical CC.

XPS is used to characterize the films' compositions because of its high sensitivity to light elements such as boron or carbon. We use the C 1*s*, Fe 2*p*, and Co 2*p* peaks of XPS (Supplemental Material S2 [25]) to study the elemental proportions in the films. Here, our $(Co_{0.5}Fe_{0.5})_xC_{1-x}$ films can be expressed as $(Co_xFe_{1-x})_yC_{1-y}$ with $x = 0.51$–0.53 and $y = 0$–0.16 (Supplemental Material S3 [25]). The slight composition deviation can be understood since the Fe and Co elements on the target surface have different ionization energies and the CC can tune the deposition rate. Moreover, except for the Ar and Ta signals in the XPS survey spectrum (not shown here), no other elements are observed, suggesting the absence of impurities and confirming the high purity of Co-Fe-C alloy films.

To directly observe the films' nanostructures changing with carbon doping, HRTEM is performed in the samples with low, medium, and high CCs, respectively. Bright field scanning transmission electron microscopy (STEM) imaging and the corresponding energy-dispersive x-ray spectroscopy mapping for each constituent element [Figs. 2(a) and 2(b)] reveal that Co, Fe, and Ta atoms are distributed homogeneously inside each layer region without any segregation at the surface or interface. The straight interfaces between the Co-Fe-C film and Ta are distinct as denoted by two yellow dotted lines. Note that the thickness of each layer is 5 nm for the underlayer Ta, 20 nm for the Co-Fe-C alloy film, and 5 nm for the capping Ta, respectively, which is consistent with the deposition rates determined by XRR. The HRTEM images of the Co-Fe-C films with CC 0% [Fig. 2(d)], 4.4% [Fig. 2(e)], and 13.2% [Fig. 2(f)] are obtained in the same region of each sample denoted by the white solid rectangle in the low-resolution image in Fig. 2(c). FFT focused on the selected zones (yellow dotted squares, note that only Co-Fe-C is included to avoid confusion from other layers) is performed to observe the nanostructure evolution with carbon doping. As shown in the respective insets of Figs. 2(d)–2(f), the transform images change from a diffraction matrix in the CC 0% to a plurality of diffraction rings involving a few dots in the CC 4.4%, and then to a weak diffraction in the CC

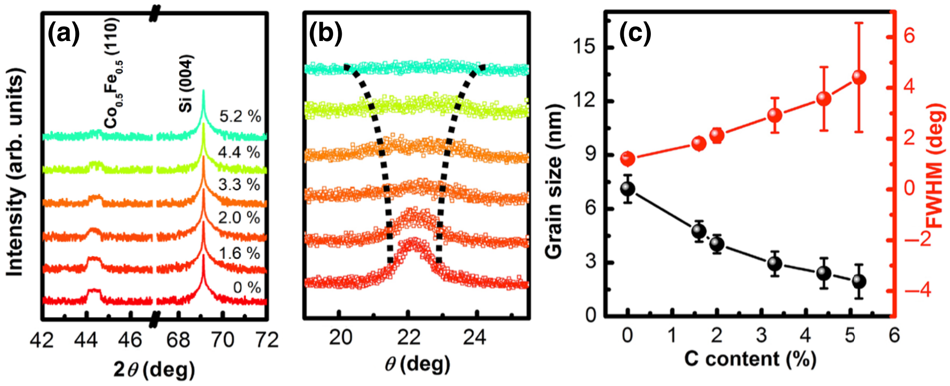

FIG. 1. Samples' structure and grain size estimation. (a) XRD pattern of $(Co_{0.5}Fe_{0.5})_xC_{1-x}$ films with $x = 0$ to 5.2%. (b) Rocking curves of the $Co_{0.5}Fe_{0.5}$ (110) reflection. FWHM is obtained using Gauss peak function fitting as dashed curves. Dotted lines are guided to show the FWHM broadening process. (c) FWHM (red balls) and grain sizes (black balls) estimations of samples with CC $x = 0$ to 5.2%.

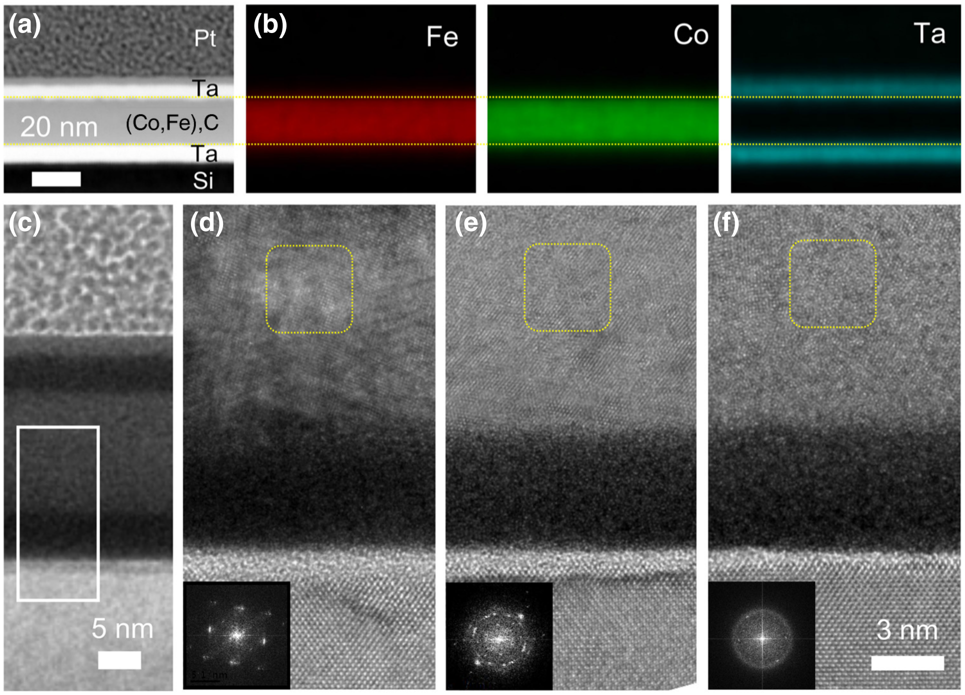

FIG. 2. Structure determination via HRTEM. (a) A bright-field STEM image of Ta/(Co, Fe)C/Ta/SiO_2/Si (001) substrate. (b) The corresponding energy-dispersive x-ray spectroscopy mappings for Fe, Co, and Ta elements, respectively. (c) Cross sections of low-resolution TEM with white solid rectangle displaying the corresponding location of HRTEM. (d)–(f) HRTEM images of Co-Fe-C alloy films with CC 0%, 4.4%, and 13.2%, respectively. The FFT of selected zones (yellow dotted squares) are inserted at the bottom left corner.

13.2%. These results verify that the Co-Fe-C films have the ordered lattice at CC 0%, the disordered amorphous at CC 13.2%, and the intermediate nanostructure at CC 4.4%.

B. Magnetostriction and piezomagnetic coefficient

The magenetostriction behavior of these Co-Fe-C films is shown in Fig. 3(a) as a function of the in-plane driving magnetic field for Co-Fe-C films with different CCs. Samples with CCs lower than 4% show no magnetostrictive response until the magnetic field reaches more than 30 Oe. With the CC increasing to greater than 4%, the responsive magnetic field to magnetostriction decreases to lower than 20 Oe and then gradually becomes smaller. The magnetostrictive behavior suggests that 4% is a critical CC to separate the films' structure into nanocrystalline and amorphous, which is consistent with the XRD results shown in Fig. 1(c). The λ_s for these Co-Fe-C films are collected as black squares in Fig. 3(b). Interestingly, the λ_s value of the binary $Co_{0.5}Fe_{0.5}$ film is 13 ppm, which is 20% of the reported value of 67 ppm [7]. The main reason for this behavior is our use of the small 20-nm-thickness samples for magnetostriction measurements, compared to a thickness of 500-nm $Co_{1-x}Fe_x$ films in Ref. [7]. A large thickness is helpful for releasing strain from lattice mismatch and forming magnetic domains and crystal boundaries in the film, leading to the magnetostriction discrepancy in samples with different thicknesses. The λ_s values first increase and reach a maximum of 75 ppm at CC 5.2%, and then drop to 27 ppm at CC 6.4%, finally gradually reducing to 10 ppm at CC 15.8%. To ensure the results are repeatable, the magnetostriction, M-H, and broadband FMR measurements of the second group of samples fabricated in the same condition are reproduced. The collected information is shown in Fig. S4 [25] for comparison.

To obtain the piezomagnetic coefficient (maximum value of $d\lambda/dH$) of the Co-Fe-C films, magnetostriction constants are derived with respect to the in-plane driving magnetic fields in Fig. 3(c). As shown by the red cycles in Fig. 3(b), a peak in the area with a CC between 4% and 6% is observed and the biggest value is 10.3 ppm/Oe at 4.8% CC. There have been some reports that the chemical and structural heterogeneity in the oxide and metallic alloy can lead to extraordinary behaviors [7,37]. Thus, a coexistence phase with a CC between 4% to 6% in these films is reasonable. We separate the CC into three parts, that is, the nanocrystalline bcc phase with CC $< 4\%$, the amorphous phase with CC $> 6\%$, and the coexistence phase with CC between 4% and 6%. The phase boundaries are marked with light orange and green dotted lines as shown in Figs. 3(b) and 3(d). The CC separation here is consistent with the grain size estimation by XRD in Fig. 1(c) and is confirmed by FFT analysis in the HRTEM images as shown in Fig. 2. It is believed that the doping metalloid atoms will form atom pairs or clusters that destabilize the parent $D0_3$ phase [38]. Therefore, the CC region of 4% to 6% is the optimized concentration for the magnetostriction behavior and piezomagnetic effect for Co-Fe-C films. It should be mentioned that the peak value of λ_s in the Co-Fe-C films is higher than the reported value in Ga-Fe-B films and is three times higher than the widely used material Co-Fe-B films. Meanwhile, the maximum

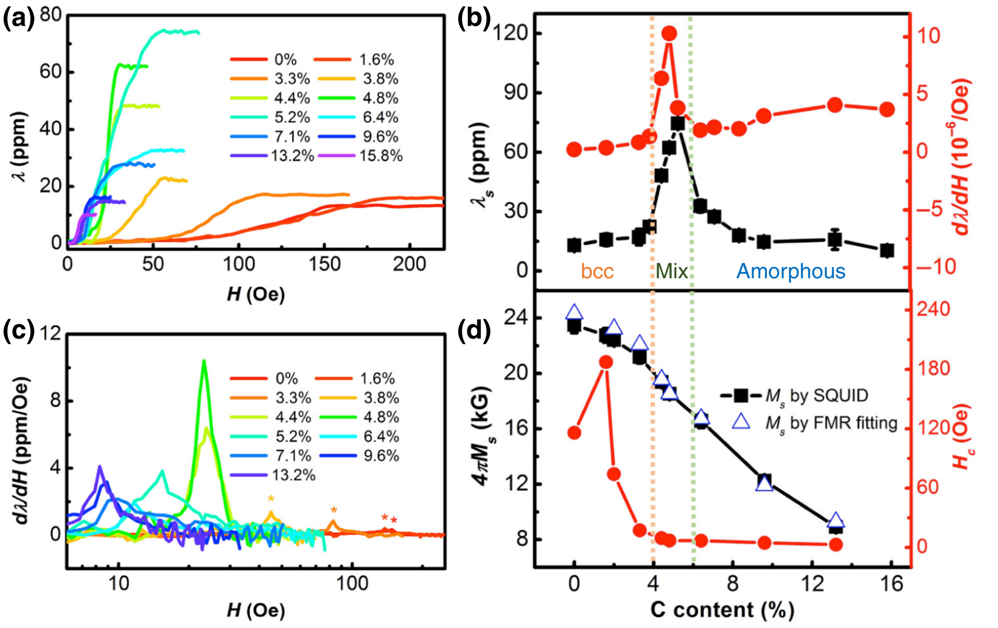

FIG. 3. Samples' magnetostriction and magnetism. (a) Magnetostriction constant of $(Co_{0.5}Fe_{0.5})_xC_{1-x}$ films with $x = 0$ to 15.8%. (b) The saturated magnetostriction constant (black) and piezomagnetic coefficient (red) with different CCs. The structural boundaries of the alloy are marked with light orange and green dotted lines. (c) Piezomagnetic coefficient versus corresponding driving magnetic field for $(Co_{0.5}Fe_{0.5})_xC_{1-x}$ films with $x = 0$ to 13.2%. (d) The M_s (black) and H_c (red) versus CC. The blue open triangles are the fitted M_s from broadband FMR measurement.

$d\lambda/dH$ is much larger than other well-known magnetostrictive materials such as Terfenol-D, Ga-Fe-B films, and Metglas [39], making these Co-Fe-C films excellent candidates for voltage-tunable magnetoelectric devices in multiferroic composite structures.

The ultraexcellent mechanical response induced by electrical and magnetic fields in the coexistence phase is universal in the piezoelectric, ferroelectric, and magnetic alloy materials [7,37,40]. For the piezoelectric and ferroelectric materials, the local structural heterogeneity triggers the competition between bulk and interfacial energies. The high mechanical response to the electric field occurs when the impact of interfacial energies is sufficiently large [37,40]. For the magnetic alloy materials, the authors thought the phase boundary played a significant role in the enhancement of the mechanical response to the magnetic field, which was evidenced in the Fe-Ga alloy system [7]. Therefore, we believe that this interfacial mechanism is closely related to our coexistence phase sample's results. However, the real microscopic origin needs further simulation and first-principles calculation.

C. Soft magnetism

Now, we explore the magnetic properties of these Co-Fe-C films. The *M-H* hysteresis loops (not shown here) scanning between $H = +1$ and -1 kOe are measured with the field applied along the MEA by the MPMS. The saturation magnetization (M_s) and coercivity (H_c) of each Co-Fe-C film are collected in Fig. 3(d). As CC increases, the M_s becomes smaller and the entire trend is nearly linear, similar to the results of Co-Fe-B [41] and Ga-Fe-B [22]. The binary $Co_{0.5}Fe_{0.5}$ film has a M_s of 23.5 kG, which is close to what has been reported by Schoen *et al.* [42]. The alloy structure transition with a carbon addition does not show an obvious influence on the M_s, but the soft magnetism of these films is dramatically improved. The H_c of these Co-Fe-C films is reduced from about 110 Oe for the binary $Co_{0.5}Fe_{0.5}$ film to about 10 Oe with CC > 4% and reaches 2 Oe at 15.8%. When the CC is less than 4%, the carbon addition cannot totally destroy the bcc lattice, but can refine the grain size, resulting in varied H_c. At a CC of 4% or higher, a carbon addition destabilizes the parent phase, turning Co-Fe-C films from nanocrystalline to amorphous. The elimination of magnetocrystalline anisotropy results in the extremely low H_c. These changes in soft magnetism are related to the structure transition with the carbon addition, which agrees with the previous XRD results. It should be noted that the H_c of the Co-Fe-C films in the nanocrystalline region first increases and reaches a maximum of about 180 Oe at a CC 1.6%, and then sharply drops. This result can be understood when combined with the FMR results.

We characterize the magnetic anisotropy of these Co-Fe-C films by VSM in order to obtain further information about the soft magnetism. Because these Co-Fe-C films do not have perpendicular anisotropy (not shown here), the large out-of-plane demagnetization field forces the magnetic moments to lie in-plane. A schematic diagram of the in-plane magnetic anisotropy measurement obtained from the VSM is shown in the inset of Fig. 4(b). The remanent magnetization ratios (M_r/M_s) along different in-plane directions with 15° or 30° intervals are obtained from the *M-H* loops to show the magnetic anisotropy. Interestingly, an in-plane uniaxial magnetic anisotropy (UMA) is observed in the Co-Fe-C films with CCs larger than 4%, shown as the blue curve in Fig. 4(a), but the films with CCs less than 4% have magnetic isotropy as the

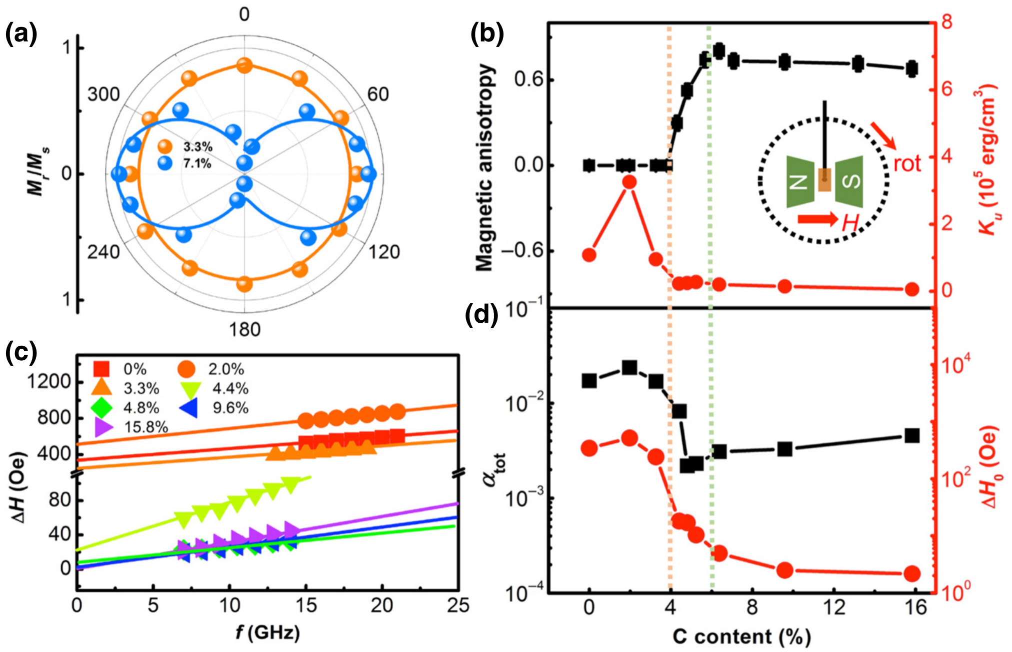

FIG. 4. Samples' magnetic anisotropy analysis and Gilbert damping. (a) In-plane angular dependence of M_r/M_s for $(\mathrm{Co}_{0.5}\mathrm{Fe}_{0.5})_x\mathrm{C}_{1-x}$ films with $x = 3.3\%$ and 7.1%, respectively. The 0° is along the MHA direction. Solid curves are theoretical fittings with a sine square function. (b) The collection of UMA coefficients A (black) and fitted UMA constants (red) from Eq. (2) of the Co-Fe-C films. The inset is the side view sketch of in-plane magnetic anisotropy measurement by VSM with magnetic field direction and sample rotation direction. The structural boundaries of the alloy are marked with light orange and green dotted lines as in Fig. 3. (c) Line width (symbols) versus frequency for samples with $x = 0$ to15.8% and fitted to Eq. (1) (solid lines) to determine both Gilbert damping α_{tot} and inhomogeneous linewidth broadening ΔH_0 in (d).

orange curve in Fig. 4(a). The M_r/M_s in the UMA can be expressed as: $M_r/M_s = A{*}\sin^2\varphi + B$, where φ is the angle between the applied magnetic field direction and MHA, and A and B are the fitting anisotropic coefficients, which are varied between 0 and 1. The coefficient A represents the intensity of the sample's UMA, as the sample is isotropic with $A = 0$, completely UMA with $A = 1$, and a superposition state of isotropic and UMA with $0 < A < 1$. The coefficient A of each Co-Fe-C film is collected as black squares in Fig. 4(b). At CCs less than 4%, the films are isotropic with $A = 0$. The value for A sharply increases from 0 to 0.8 in the coexistence phase and then gradually decreases in the amorphous phase. These films are superposition states with $0 < A < 1$. The CC-dependent features of coefficient A have a similar evolution trend as the UMA constant (K_u) except in the nanocrystalline bcc phase, which will be mentioned later.

The origin of the UMA can be attributed to magnetocrystalline anisotropy, induced anisotropy, interfacial charge transfer, and the strain effect [43]. We first rule out the induced anisotropy due to the absence of a magnetic field during deposition. There have been some reports on the UMA induced by substrate surface topography [44]. However, the silicon- (001) oriented substrate did not show any special topography such as strip or step (not shown here), indicating the UMA is not related in this scenario. The interfacial charge transfer also cannot be the reason for UMA in these films due to the inserted metallic seed layer Ta between the substrate and Co-Fe-C films. The thickness of the Ta layer is 5 nm, well above the electric field screening length (1–2 unit cells). Therefore, the UMA could be from the films' magnetocrystalline anisotropy and strain effect. For the films with CC > 6%, the UMA from magnetocrystalline anisotropy can be excluded due to its absence in amorphous films. The strain effect from the silicon substrate could be the only reason for the UMA. The underlayer Ta thickness-dependent magnetic anisotropy analysis is carried out to further verify the strain effect in the Supplemental Material S5 [25]. So far, we believe the residual stress from substrate cutting could contribute to the amorphous films' UMA. For the films with CC < 4%, there is a magnetic anisotropy competition between magnetocrystalline anisotropy and the strain effect. However, the magnetocrystalline anisotropy is 10–100 times larger than the strain effect in these films (detailed calculations are in the Supplemental Material S6 [25]), suggesting the dominant contribution is from magnetocrystalline anisotropy. Since these films are polycrystalline here, the magnetocrystalline anisotropy in each grain randomly distributes, making the films isotropic. It is much more complicated for the films in the coexistence phase. The carbon addition here destroys the bcc structure and destabilizes the parent phase. The collapse of the parent structure eliminates the magnetocrystalline anisotropy contribution and brings in the strain effect.

D. Microwave properties

Broadband FMR measurement is carried out with an external magnetic field applied parallel to the MEA. The narrow FMR line width at the X band (25 Oe in Fig. S7 [25]) is achieved in the sample with a CC of 4.8%. Figure 4(c) shows the curves of absorbed line width (ΔH) versus resonant frequency (f) with CCs ranging from 0% to 15.8%. A linear fitting is applied to each sample using the relation [45]

$$\Delta H(f) = \frac{4\pi\alpha_{\text{tot}}}{\gamma} f + \Delta H_0, \tag{1}$$

where γ is the electron gyromagnetic ratio, α_{tot} is the total Gilbert damping constant, and ΔH_0 is the inhomogeneous line width broadening at 0 Hz. As shown in Fig. 4(d), in the nanocrystalline phase, both α_{tot} and ΔH_0 are maximum at CC 1.6%. Then α_{tot} and ΔH_0 sharply decrease to 0.002 and 10 Oe, respectively, when carbon doping reaches the coexistence phase. In the amorphous phase, α_{tot} gradually increases and ΔH_0 decreases with CC increasing. There have been some reports that the in-plane total damping is the sum of the intrinsic and extrinsic damping, where the extrinsic part arises from the spin pumping and two-magnon scattering [46]. But the total extrinsic contribution is about 10^{-3} [45], which will not dominate the CC-dependent features in total damping. The minimum α_{tot} here is 0.002, indicating that the minimum of intrinsic damping of these Co-Fe-C films is about 0.001, better than the reported value of 0.004 in $\text{Co}_{0.4}\text{Fe}_{0.4}\text{B}_{0.2}$ film [47]. There are only a limited number of reports for composition analysis of ΔH_0. For $\text{Co}_x\text{Fe}_{1-x}$ alloys, the value of ΔH_0 is related to the number of defects of the films [48] and uniformity of the structure phase [49]. We consider the same factors in these Co-Fe-C films as they have the same parent phase. The relatively large ΔH_0 in the nanocrystalline phase compared to the other phases is caused by the large number of multicrystal boundaries (a type of structure defect). The sharp decrease of ΔH_0 in the coexistence phase is attributed to the same phase that remains intermixed throughout the transition, but not the segregation near the phase transition as suggested by Schoen *et al.* [49]. The in-plane M_s and K_u can be fitted using [50]

$$(\omega/\gamma)^2 = (H + 2K_u/M_s)(H + 4\pi M_s + 2K_u/M_s), \tag{2}$$

where Eq. (2) is used when H is applied along MEA in the UMA samples. The fitted $\gamma/2\pi = 29.5 \pm 1.0$ GHz/T is consistent with the reported value [48]. The fitted M_s of samples are shown as the blue open triangles in Fig. 3(d), which agree well with the measured values. The K_u is marked with red circles in Fig. 4(b). Interestingly, the K_u is not 0 in the nanocrystalline phase, different from the previous anisotropic coefficient A's features. It can be understood that anisotropic coefficient A is from the M-H loops measurement, representing the macroscopic anisotropy. However, K_u is from resonant field fitting of FMR, representing the intrinsic anisotropy. Based on the strong crystallization evidence in XRD, FFT in HRTEM, and relatively large H_c and ΔH_0 in the low CC samples, it is believed that the macroscopic isotropy is due to a random distribution of respective magnetocrystalline anisotropic axes that exist in each grain. Hence, the fitted large K_u in the nanocrystalline phase indicates the average magnetocrystalline anisotropy of all grains. Interestingly, the fitted K_u in the low CC samples reaches 10^5 erg/cm^3, which is 10 times more than the value of the amorphous samples. This result is consistent with what we have mentioned in the intensity comparison of magnetocrystalline anisotropy and strain effect. With carbon doping, the magnetocrystalline anisotropy is continuously damaged in the nanocrystalline and coexistence phase, resulting in the sharp decrease of K_u. For the amorphous phase, the magnetocrystalline anisotropy is eliminated and the uniform amorphous proportion is enhanced with the carbon addition, leading to K_u continuing to gradually decrease. The maximum K_u at CC 2% will be discussed later. Thus, K_u is strongly influenced by the alloy structural transition with the carbon addition.

E. Thermal stability of magnetic properties

To test the thermal stability of the Co-Fe-C alloy films, three different samples with CCs 0%, 4.4%, and 13.2% are annealed at the same temperature for 1 h in a continuous Ar gas flow. All samples show the increased M_s with increasing annealing temperature [Fig. 5(a)], the same as the reported results in Co-Fe-B alloy films [51,52] marked by solid balls in Fig. 5(a). Considering the elements' C and B similarities, this behavior can be understood by the elements' interdifussion, which occurs during the annealing as explained by Wang *et al.* [52]. During the annealing above the critical temperature, carbon atoms might diffuse away from Co-Fe-C at the interface, resulting in the reduction of magnetic impurities (carbon atoms), and therefore, increase the magnetic moment. Since the size of a carbon atom is much smaller than that of the other atoms (Co, Fe, and Ta), carbon diffusion must be easier and faster than other atoms, and therefore, dominates the magnetization variation during annealing. The net varied M_s is defined as $\Delta 4\pi M_s = 4\pi M_s\ (\text{T}) - 4\pi M_s\ (0)$, where $4\pi M_s$ (0) is the saturated magnetic moment without annealing. The calculated curves are shown in Fig. 5(c), from which one can see all three samples are thermally stable up to

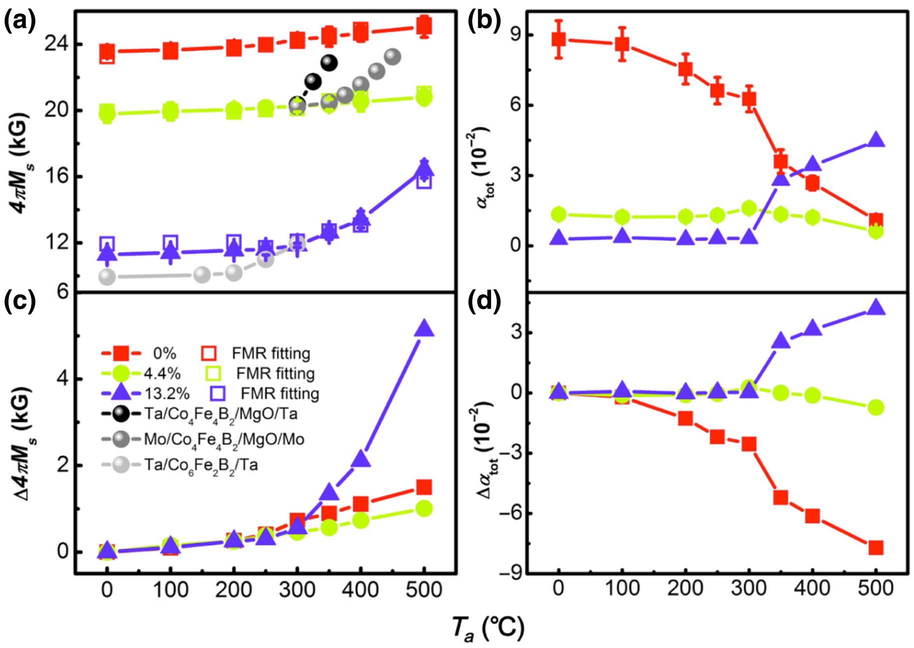

FIG. 5. Thermal stability of Co-Fe-C films with CC 0%, 4.4%, and 13.2%. Annealing temperature-dependent M_s (a) and α_{tot} (b). The Co-Fe-B alloy film's M_s after annealing in the references are collected for comparison as solid balls in (a). The net varied M_s (c) and α_{tot} (d) after annealing.

250 °C. The apparent M_s increase in CC 13.2% and the minimal M_s increase in CC 4.4% are observed at the range of 250 °C–500 °C. Overall, the annealing temperature-dependent M_s of Co-Fe-C alloy films show better thermal stability than that of the Co-Fe-B alloy films, which agrees well with the reported works [19,20].

The respective α_{tot} of the three samples after annealing and the corresponding net varied values are displayed in Figs. 5(b) and 5(d). Interestingly, the sample with CC 0% shows a continuous reduction of α_{tot} in the whole annealing range. The α_{tot} of the sample with CC 13.2% is thermally stable up to 300 °C, then sharply jumps to a high value, and finally continues to gradually increase. These microwave properties that change after annealing are consistent with Bilzer's work [53] in the Co-Fe-B alloy films. However, the medium doping sample with CC 4.4% shows the maximum thermal tolerance, from which no apparent alteration of α_{tot} is shown in the whole annealing range. Based on the above discussion, the Co-Fe-C alloy film with a coexistence phase has the best thermal stability among all the samples. It is certain that the varied magnetic properties after annealing depend strongly on the transformation of the films' nanostructures. Further investigation is in process to understand the internal mechanism.

F. Electronic structure calculation

Ebert *et al.* [54] and Lounis *et al.* [55] suggested that the intrinsic damping is proportional to the total density of states (DOS) at the Fermi energy [$n(E_F)$] in the breathing Fermi-surface model (as in the case for the Co_xFe_{1-x} system [45]). Thus, we perform electronic structure calculations for the Co-Fe-C alloy to gain a deeper understanding of the relation between Gilbert damping and CC. The schematic bcc structure of the Co-Fe-C alloy is shown in Fig. 6(a). With the carbon addition, the local distortion of the positions of the Fe or the Co atom near the interstitial C atoms can be clearly observed. The periodic cell used for calculation is marked as a dashed line. The detailed description of the calculation method is in the Supplemental Material S8 [25]. A CC less than 6% is employed in our calculation considering the nanocrystalline bcc structure. Several representative examples are given in Fig. 6(d). The 3*d* states (valley in the DOS below E_F) change obviously, but do not shift with a CC increase. Focusing on the DOS around E_F [inset of Fig. 6(d)] clearly shows that the CC-dependent features in $n(E_F)$ directly correlate to features related to damping as shown in Fig. 6(b). The calculated M_s of each supercell is collected to compare with the measured M_s in Fig. 6(c). The initial increase of $n(E_F)$ with CC < 2% is related to the carbon doping effect on the band splitting of the metal ferromagnetism introduced in the Stoner criterion [6]. This low-content doping tunes the magnetic properties of alloys such as H_c, K_u, and intrinsic damping as shown in the previous data. Then, $n(E_F)$ decreases with CC > 2%, originating from the strong hybridization between C 2*p* states and Fe or Co 3*d* states, which localize the electrons around the E_F of the alloy. The extremely low Gilbert damping that we measure is related to the minimum in $n(E_F)$ for CC around 5%, at which the doping of carbon atoms optimally hybridizes with the surrounding metal Fe or Co atoms [45]. Additional work is being done to investigate the mechanism of the $n(E_F)$ turning point happening at a CC around 2%. All the calculations are carried out in the periodic supercell. The unit cell destruction from carbon

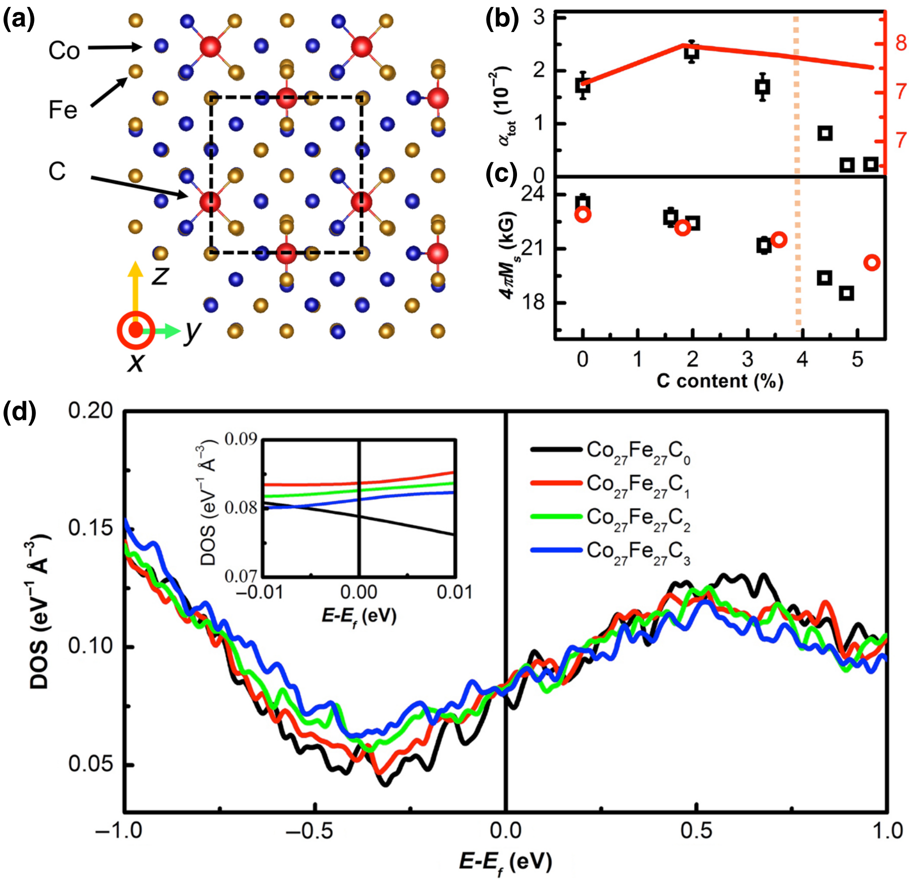

FIG. 6. DOS calculation for Co-Fe-C films with CC less than 6%. (a) Side view of schematic structure of interstitial C atoms (red balls) in the bulk $Co_{0.5}Fe_{0.5}$ alloy. The radius of C atoms is amplified for clearness. The Fe and Co atoms are represented by gold and blue balls, respectively. The dashed line show the Co-Fe-C supercell employed in our calculation. (b) The measured α_{tot} (black open) and the calculated $n(E_F)$ (red curve). (c) The comparison of measured M_s (black open) and calculated M_s (red open). The light orange dotted line is the structural boundary as in Fig. 3. (d) Electronic structure of bulk $(Co_{0.5}Fe_{0.5})_xC_{1-x}$ with $x < 6\%$. All alloy compositions are aligned to a common Fermi energy E_F, at zero energy to facilitate comparison. The inset is the DOS enlargement around E_F.

doping is not considered in the calculation, which may lead to disagreement between the calculated $n(E_F)$ and the M_s with the measured damping and the M_s that varies near the structure boundary.

IV. CONCLUSION

In summary, we study the magnetostriction, soft magnetism, and microwave properties of different CC concentrations in $(Co_{0.5}Fe_{0.5})_xC_{1-x}$ films grown on silicon (001) substrates. Three distinct CC regions are identified: below 4%, the phase is primarily nanocrystalline bcc, above 6%, the phase is primarily amorphous, and between 4% and 6%, there is mixture of nanocrystalline and amorphous. A combination of high λ_s, high $d\lambda/dH$, low H_c, narrow FMR line width, low α_{tot} and high thermal stability are achieved. The large λ_s and $d\lambda/dH$ are related to the coexistence of nanocrystalline bcc and the amorphous phase. The extremely low damping is related to the minimum in $n(E_F)$ of the alloys that is induced by carbon doping. We also analyze the competition between magnetocrystalline anisotropy and strain effects in determining the magnetic anisotropy of the Co-Fe-C films. This work will stimulate the Co-Fe-C films' applications in voltage-tunable magnetoelectric devices in multiferroic composite structures and other microwave magnetic devices.

ACKNOWLEDGMENTS

This work was supported by the state scholarship fund of China Scholarship Council (Grant No. 201607285003), National Natural Science Foundation of China (NSFC) (Grants No. 11504327, No. 11504326, and No. 11774195), Zhejiang Provincial Natural Science Foundation of China (Grants No. LQ15A040002 and No. LQ19F010005), Open Project Funding of the Key Laboratory of Electromagnetic Wave Information Technology and Metrology of Zhejiang Province (Grant No. 2019KF0002), Scientific Research Foundation of Zhejiang University of Technology and in part by the National Science Foundation TANMS ERC Grant No. 1160504. The magnetization work was supported by the National Science Foundation Grant No. ECCS-1402738. The authors wish to thank Dr. S. Zhang for his constructive suggestions and discussions.

[1] C. Chappert, A. Fert, and F. N. V. Dau, The emergence of spin electronics in data storage, Nat. Mater. **6**, 813 (2007).

[2] D. Houssameddine, U. Ebels, B. Delaët, B. Rodmacq, I. Firastrau, F. Ponthenier, M. Brunet, C. Thirion, J.-P. Michel, L. Prejbeanu-Buda, M.-C. Cyrille, O. Redon, and B. Dieny, Spin-torque oscillator using a perpendicular polarizer and a planar free layer, Nat. Mater. **6**, 447 (2007).

[3] T. Maruyama, Y. Shiota, T. Nozaki, K. Ohta, N. Toda, M. Mizuguchi, A. A. Tulapurkar, T. Shinjo, M. Shiraishi, S. Mizukami, Y. Ando, and Y. Suzuki, Large voltage-induced magnetic anisotropy change in a few atomic layers of iron, Nat. Nanotechnol. **4**, 158 (2009).

[4] D. Chiba, S. Fukami, K. Shimamura, N. Ishiwata, K. Kobayashi, and T. Ono, Electrical control of the ferromagnetic phase transition in cobalt at room temperature, Nat. Mater. **10**, 853 (2011).

[5] Y. Kakehashi, *Modern Theory of Magnetism in Metals and Alloys* (Springer, Berlin, 2012), pp. 203–206.

[6] J. M. D. Coey, *Magnetism and Magnetic Materials* (Cambridge University Press, Cambridge, 2014), pp. 150–152, 134–135, 384–387.

[7] D. Hunter, W. Osborn, K. Wang, N. Kazantseva, J. Hattrick-Simpers, R. Suchoski, R. Takahashi, M. L. Young, A. Mehta, L. A. Bendersky, S. E. Lofland, M. Wuttig, and I. Takeuchi, Giant magnetostriction in annealed $Co_{1-x}Fe_x$ thin-films, Nat. Commun. **2**, 518 (2011).

[8] C. A. Bauer and P. E. Wigen, Spin-wave resonance studies in invar films, Phys. Rev. B **5**, 4516 (1972).

[9] A. J. P. Meyer and G. Asch, Experimental g' and g values of Fe, Co, Ni, and their alloys, J. Appl. Phys. **32**, S330 (1961).

[10] R. A. Reck and D. L. Fry, Orbital and spin magnetization in Fe-Co, Fe-Ni, and Ni-Co, Phys. Rev. **184**, 492 (1969).

[11] D. D. Djayaprawira, K. Tsunekawa, M. Nagai, H. Maehara, S. Yamagata, N. Watanabe, S. Yuasa, Y. Suzuki, and K. Ando, 230% room-temperature magnetoresistance in CoFeB/MgO/CoFeB magnetic tunnel junctions, Appl. Phys. Lett. **86**, 092502 (2005).

[12] S. Yuasa, Y. Suzuki, T. Katayama, and K. Ando, Characterization of growth and crystallization processes in CoFeB/MgO/CoFeB magnetic tunnel junction structure by reflective high-energy electron diffraction, Appl. Phys. Lett. **87**, 242503 (2005).

[13] S. Chikazumi, *Physics of Ferromagnetism* (Syokabo, Tokyo, 1978), Vol. 1, p. 260.

[14] S. U. Jen, Y. D. Yao, Y. T. Chen, J. M. Wu, C. C. Lee, T. L. Tsai, and Y. C. Chang, Magnetic and electrical properties of amorphous CoFeB films, J. Appl. Phys. **99**, 053701 (2006).

[15] T. Kubota, T. Daibou, M. Oogane, Y. Ando, and T. Miyazaki, Tunneling spin polarization and magnetic properties of Co-Fe-B alloys and their dependence on boron content, Jpn. J. Appl. Phys. **46**, L250 (2007).

[16] S. Ikeda, J. Hayakawa, Y. Ashizawa, Y. M. Lee, K. Miura, H. Hasegawa, M. Tsunoda, F. Matsukura, and H. Ohno, Tunnel magnetoresistance of 604% at 300 K by suppression of Ta diffusion in CoFeB/MgO/CoFeB pseudo-spin-valves annealed at high temperature, Appl. Phys. Lett. **93**, 082508 (2008).

[17] T. Kawahara, K. Ito, R. Takemura, and H. Ohno, Spin-transfer torque RAM technology: Review and prospect, Microelectron. Reliab. **52**, 613 (2012).

[18] S. Ikeda, K. Miura, H. Yamamoto, K. Mizunuma, H. D. Gan, M. Endo, S. Kanai, J. Hayakawa, F. Matsukura, and H. Ohno, A perpendicular-anisotropy CoFeB-MgO magnetic tunnel junction, Nat. Mater. **9**, 721 (2010).

[19] A. A. El-Gendy, M. Bertino, D. Clifford, M. Qian, S. N. Khanna, and E. E. Carpenter, Experimental evidence for the formation of $CoFe_2C$ phase with colossal magnetocrystalline-anisotropy, Appl. Phys. Lett. **106**, 213109 (2015).

[20] S. Chen, J. Zhou, W. Lin, J. Yu, R. Guo, F. Poh, D. Shum, and J. Chen, Ferromagnetic alloy material CoFeC with high thermal tolerance in MgO/CoFeC/Pt structure and comparable intrinsic damping factor with CoFeB, J. Phys. D: Appl. Phys. **51**, 055006 (2018).

[21] A. P. Chen, J. D. Burton, E. Y. Tsymbal, Y. P. Feng, and J. Chen, Effects of B and C doping on tunneling magnetoresistance in CoFe/MgO magnetic tunnel junctions, Phys. Rev. B **98**, 045129 (2018).

[22] J. Lou, R. E. Insignares, Z. Cai, K. S. Ziemer, M. Liu, and N. X. Sun, Soft magnetism, magnetostriction, and microwave properties of FeGaB thin films, Appl. Phys. Lett. **91**, 182504 (2007).

[23] P. Li, A. Chen, D. Li, Y. Zhao, S. Zhang, L. Yang, Y. Liu, M. Zhu, H. Zhang, and X. Han, Electric field manipulation of magnetization rotation and tunneling magnetoresistance of magnetic tunnel junctions at room temperature, Adv. Mater. **26**, 4320 (2014).

[24] C. Dong, M. Li, X. Liang, H. Chen, H. Zhou, X. Wang, Y. Gao, M. E. McConney, J. G. Jones, G. J. Brown, B. M. Howe, and N. X. Sun, Characterization of magnetomechanical properties in FeGaB thin films, Appl. Phys. Lett. **113**, 262401 (2018).

[25] See the Supplemental Material at http://link.aps.org/supplemental/10.1103/PhysRevApplied.12.034011 which include Refs. [[26–35]], for further information concerning XRD analysis, XPS spectra, repeatable measurements for the second group of samples for comparison, underlayer thickness-dependent soft magnetism, K_u calculation, narrow line width in FMR spectra, and description of electronic structure calculation.

[26] J. Stöhr and H. C. Siegmann, *Magnetism From Fundamentals to Nanoscale Dynamics, Springer Series in Solid-State Sciences* (Springer, Berlin, 2006), pp. 385–388.

[27] C. T. Chen, Y. U. Idzerda, H.-J. Lin, N. V. Smith, G. Meigs, E. Chaban, G. H. Ho, E. Pellegrin, and F. Sette, Experimental Confirmation of the X-Ray Magnetic Circular Dichroism Sum Rules for Iron and Cobalt, Phys. Rev. Lett. **75**, 152 (1995).

[28] A. S. Aricò, A. K. Shuklab, H. Kimc, S. Parkc, M. Minc, and V. Antonuccia, An XPS study on oxidation states of Pt and its alloys with Co and Cr and its relevance to electroreduction of oxygen, Appl. Surf. Sci. **172**, 33 (2001).

[29] C. A. F. Vaz, Electric field control of magnetism in multiferroic heterostructures, J. Phys. Condens. Matter **24**, 333201 (2012).

[30] A. Mardana, S. Ducharme, and S. Adenwalla, Ferroelectric Control of Magnetic Anisotropy, Nano Lett. **11**, 3862 (2011).

[31] G. Kresse and J. Furthmuller, Efficiency of ab-initio total energy calculations for metals and semiconductors using a plane-wave basis set, Comput. Mater. Sci. **6**, 15 (1996).; Efficient iterative schemes for ab initio total-energy calculations using a plane-wave basis set, Phys. Rev. B **54**, 11169 (1996).

[32] J. P. Perdew, K. Burke, and M. Ernzerhof, Generalized Gradient Approximation Made Simple, Phys. Rev. Lett. **77**, 3865 (1996).

[33] G. Kresse and D. Joubert, From ultrasoft pseudopotentials to the projector augmented-wave method, Phys. Rev. B **59,** 1758 (1999).

[34] H. J. Monkhorst and J. D. Pack, Special points for Brillouin-zone integrations, Phys. Rev. B **13**, 5188 (1976).

[35] A. L. Patterson, The Scherrer formula for X-ray particle size determination, Phys. Rev. **56**, 978 (1939).

[36] N. X. Sun and K. Lu, Grain-size limit of polycrystalline materials, Phys. Rev. B **59**, 5987 (1999).

[37] F. Li, D. Lin, Z. Chen, Z. Cheng, J. Wang, C. Li, Z. Xu, Q. Huang, X. Liao, L.-Q. Chen, T. R. Shrout, and S. Zhang, Ultrahigh piezoelectricity in ferroelectric ceramics by design, Nat. Mater. **17**, 349 (2018).

[38] A. E. Clark, J. B. Restorff, M. Wun-Fogle, K. B. Hathaway, T. A. Lograsso, M. Huang, and E. Summers, Magnetostriction of ternary Fe-Ga-X (X = C, V, Cr, Mn, Co, Rh) alloys, J. Appl. Phys. **101**, 09C507 (2007).

[39] J. Lou, M. Liu, D. Reed, Y. Ren, and N. X. Sun, Giant electric field tuning of magnetism in novel multiferroic FeGaB/lead zinc niobate-lead titanate (PZN-PT) heterostructures, Adv. Mater. **21**, 4711 (2009).

[40] J. X. Zhang, B. Xiang, Q. He, J. Seidel, R. J. Zeches, P. Yu, S. Y. Yang, C. H. Wang, Y.-H. Chu, L. W. Martin, A. M. Minor, and R. Ramesh, Large field-induced strains in a lead-free piezoelectric material, Nat. Nanotechnol. **6**, 98 (2011).

[41] M. Munakata, S.-I. Aoqui, and M. Yagi, B-concentration dependence on anisotropy field of CoFeB thin film for gigahertz frequency use, IEEE Trans. Magn. **41**, 3262 (2005).

[42] M. A. W. Schoen, J. Lucassen, H. T. Nembach, T. J. Silva, B. Koopmans, C. H. Back, and J. M. Shaw, Magnetic properties of ultrathin 3d transition-metal binary alloys. I. Spin and orbital moments, anisotropy, and confirmation of Slater-Pauling behavior, Phys. Rev. B **95**, 134410 (2017).

[43] J. W. Wang, *et al.*, Ferroelectric-domain-controlled magnetic anisotropy in $Co_{40}Fe_{40}B_{20}/YMnO_3$ multiferroic heterostructure, Appl. Phys. Lett. **102**, 102906 (2013).

[44] A. Berger, U. Linke, and H. P. Oepen, Symmetry-Induced Uniaxial Anisotropy in Ultrathin Epitaxial Cobalt Films Grown on Cu (1113), Phys. Rev. Lett. **68**, 839 (1992).

[45] M. A. W. Schoen, D. Thonig, M. L. Schneider, T. J. Silva, H. T. Nembach, O. Eriksson, O. Karis, and J. M. Shaw, Ultra-low magnetic damping of a metallic ferromagnet, Nat. Phys. **12**, 839 (2016).

[46] P. Omelchenko, E. A. Montoya, C. Coutts, B. Heinrich, and E. Girt, Tunable magnetization and damping of sputter-deposited, exchange coupled Py/Fe bilayers, Sci. Rep. **7**, 4861 (2017).

[47] X. Liu, W. Zhang, M. J. Carter, and G. Xiao, Ferromagnetic resonance and damping properties of CoFeB thin films as free layers in MgO-based magnetic tunnel junctions, J. Appl. Phys. **110**, 033910 (2011).

[48] A. J. Lee, J. T. Brangham, Y. Cheng, S. P. White, W. T. Ruane, B. D. Esser, D. W. McComb, P. C. Hammel, and F. Yang, Metallic ferromagnetic films with magnetic damping under $1.4*10^{(3}$, Nat. Commun. **8**, 234 (2017).

[49] M. A. W. Schoen, J. Lucassen, H. T. Nembach, B. Koopmans, T. J. Silva, C. H. Back, and J. M. Shaw, Magnetic properties of ultrathin 3d transition-metal binary alloys. II. Experimental verification of quantitative theories of damping and spin pumping, Phys. Rev. B **95**, 134411 (2017).

[50] O. Kohmoto, Effective demagnetizing factors in ferromagnetic resonance equations, J. Magn. Magn. Mater. **262**, 280 (2003).

[51] T. Liu, Y. Zhang, J. W. Cai, and H. Y. Pan, Thermally robust Mo/CoFeB/MgO trilayers with strong perpendicular magnetic anisotropy, Sci. Rep. **4**, 5895 (2014).

[52] Y. Wang, W. Chen, S. Yang, K. Shen, C. Park, M. Kao, and M. Tsai, Interfacial and annealing effects on magnetic properties of CoFeB thin films, J. Appl. Phys. **99**, 08M307 (2006).

[53] C. Bilzer, T. Devolder, J. V. Kim, G. Counil, C. Chappert, C. Cardoso, and P. P. Freitas, Study of the dynamic magnetic properties of soft CoFeB films, J. Appl. Phys. **100**, 053903 (2006).

[54] H. Ebert, S. Mankovsky, D. Ködderitzsch, and P. J. Kelly, Ab Initio Calculation of the Gilbert Damping Parameter via the Linear Response Formalism, Phys. Rev. Lett. **107**, 66603 (2011).

[55] S. Lounis, M. d, S. Dias, and B. Schweflinghaus, Transverse dynamical magnetic susceptibilities from regular static density functional theory: Evaluation of damping and g shifts of spin excitation, Phys. Rev. B **91**, 104420 (2015).